Surface & Coatings Technology 484 (2024) 130813

Contents lists available at ScienceDirect

Surface & Coatings Technology

journal homepage: www.elsevier.com/locate/surfcoat

Exploring tribological characteristics of ZrN-MoSN composite films fabricated via RF magnetron sputtering: Insights from microstructure and performance analysis

Jing Luan [a,b,f,1], Hongying Lu [a,1], Junhua Xu [a], Filipe Fernandes [b,c,f], Manuel Evaristo [b,f], Bingyang Ma [d], Fuxiang Xie [e], Albano Cavaleiro [b,f], Hongbo Ju [a,b,e,f,*]

[a] Jiangsu University of Science and Technology, School of Materials Science and Engineering, Mengxi Road 2, Zhenjiang, Jiangsu Province 212003, China
[b] University of Coimbra, CEMMPRE, ARISE, Department of Mechanical Engineering, Rua Luís Reis Santos, 3030-788 Coimbra, Portugal
[c] CIDEM, ISEP - Polytechnic of Porto, Rua Dr. António Bernardino de Almeida, 4249-015, Porto, Portugal
[d] School of Materials Science, Shanghai Dianji University, Shanghai 200240, China
[e] Weifang University, School of Machinery and Automation, Laboratory for Sustainable Surface Engineering of Agricultural Machinery Systems, Dongfeng Road 5147, Weifang, Shandong Province 261061, China
[f] University of Coimbra, ARISE, Department of Mechanical Engineering, Rua Luís Reis Santos, 3030-788 Coimbra, Portugal

ARTICLE INFO

Keywords:
RF magnetron sputtering
ZrN-MoSN films
Mechanical properties
Tribological properties

ABSTRACT

Achieving the stringent demands of sustainable tribological industrial applications poses a significant challenge, particular in optimizing the self-lubricant performance of nitride-based films. This paper tackled this challenge by designing and depositing a series of ZrN-MoSN composite films with varying (Mo + S)/Zr ratios, employing RF magnetron sputtering, aimed to enhance the tribological properties through utilizing the high loading capacity of the ZrN matrix and the exceptional self-lubricating attributes of Mo-S-N additives. After conducting thorough investigations on the microstructure, and tribological properties, the results revealed that the dense columnar structured ZrN-MoSN composite films displayed a polycrystalline composition comprising fcc-ZrN and hcp-MoS_2 phases, intertwined with amorphous phases of Mo(SN)$_x$ and $MoS_2(N_2)$. (Mo + S)/Zr ratios below 1.08 exhibited a minor impact on the room temperature (RT) tribological properties, while higher ratios led to degradation on RT average friction coefficient (COF) and wear rate (WR). However, the synergistic effect of ZrN matrix and the tribo-phases of layered MoO_3 and hard ZrO_2 contributed to the significant enhanced 500 °C tribological properties, particularly with an optimized (Mo + S)/Zr ratio of 0.43.

1. Introduction

In recent decades, the pursuit of improving the friction and wear properties of vital mechanical components via surface modification technology has become a focal point in tribology. This endeavor seeks to elevate energy transfer efficiency, prolong operational lifespan, and eradicate the necessity for environmentally detrimental lubricant/greases. This crucial important approach tackles issues linked to resource depletion and climate change, concurrently mitigating the detrimental effects of excessive energy consumption [1–4].

As scientific inquiry continues to advance, particular attention has been directed towards refining surface modification methods aimed at improving tribological properties. Notably, within the realm of physical vapor deposition technology, there has been a rapid evolution in the development of nitride ceramic-based thin film materials [5,6]. Among these materials, TiN has emerged as a standout due to its exceptional attributes and wide-ranging applicability [7–9]. However, ZrN-based films, renowned for their superior corrosion resistance and robust strength and toughness, are better suited to meet the stringent performance demands of challenging operating conditions, such as those characterized by high salt content, elevated temperatures, and heavy loads [10–12]. Accordingly, they have risen to prominence as another critical category of hard film materials. Previous studies have underscored the promising application prospects of ZrN-based thin film

* Corresponding author at: Jiangsu University of Science and Technology, School of Materials Science and Engineering, Mengxi Road 2, Zhenjiang, Jiangsu Province 212003, China.
E-mail addresses: hbju@just.edu.cn, hju@uc.pt (H. Ju).
[1] The co-first author.

https://doi.org/10.1016/j.surfcoat.2024.130813
Received 24 March 2024; Received in revised form 17 April 2024; Accepted 18 April 2024
Available online 19 April 2024

materials across various domains, ranging from the efficient cutting of hard-to-machine metals and corrosion protection in marine environments [13]. Nevertheless, the high friction coefficient associated with ZrN films restricts its broader application in the field of lubrication [14]. To address this limitation while retaining the high load-bearing capacity of ZrN-based films, the addition of soft metals offers a viable solution [15,16]. For instance, ZrN-Cu and ZrN-Ag films demonstrated superior friction-reducing properties compared to the binary ZrN films [17].

Therefore, based on diversified film design ideas, incorporating lubricating components to the ZrN film presents an effective strategy to improve the friction-reducing performance of the film [18]. Transition metal sulfides, represented by MoS_2 and WS_2, renowned for their weak interlayer van der Waals forces, serve as ideal lubricants and find extensive applications in vacuum environments, notably in the aerospace industry [19–21]. To mitigate their susceptibility to failure in atmospheric conditions, a non-metal element, nitrogen, was introduced into transition metal sulfides using via physical vapor deposition techniques [22]. This approach was inspired by significant enhancements observed in friction and wear performances within the 200 to 500 °C range upon the nitrogen addition into WS_2 film materials [23]. Additionally, our investigation underscores the pivotal role of nitrogen content in influencing the friction and wear properties of Mo-S-N films, demonstrating a substantial enhancement in wear resistance of MoS_2 films in atmospheric environments [24].

Based on the above mentioned, there is a compelling rationale to explore the synergistic benefits of compounding Mo-S-N film with ZrN film. Such an approach holds the potential to combine the high load-bearing capacity characteristic of the ZrN phase with the friction-reducing properties inherent in Mo-S-N. Consequently, this study embarked on the preparation of a series of ZrN-MoSN composite films through reactive magnetron sputtering. The investigation aimed to elucidate the impact of the (Mo + S)/Zr ratio on the microstructure, mechanical, and tribological properties of the films, with the objective of identifying the optimal parameters for maximizing film performance, marking a significant advancement in the field of self-lubricant film materials.

2. Experimental details

2.1. Film deposition

A series of ZrN-MoSN composite films were deposited on two types of substrates, namely wafer silicon and mirror-polished W18C4V (W18) with a roughness below 0.05 μm, utilizing an RF magnetron co-sputtering system. High-purity separate targets of Zr (99.9 %) and MoS_2 (99.8 %), with a diameter of 75 mm, were employed for the deposition process. The 3D schematic depiction of the deposition machine is illustrated in Fig. 1. Before deposition, all substrates underwent ultrasonic cleaning in alcohol for 15 min, followed by a 15-minute cleaning in acetone. Subsequently, the blow-dried substrates were placed into the substrate holder, maintaining a distance of 80 mm from the targets. Once the basic pressure dropped below 6×10^{-4} Pa, pure Ar gas was introduced into the chamber at a flow rate of 50 sccm, maintaining a pressure of 0.3 Pa. The targets were then powered at 50 W for 15 min to eliminate contaminants on their surfaces. A Zr interlayer, approximately 150 nm thick, was deposited on the substrates by closing the shutter in front of MoS_2 (50 W) and opening the one in front of Zr (50 W). Subsequently, nitrogen gas was introduced into the chamber at a flow rate of 1.6 sccm, while maintaining a pressure of 0.3 Pa. The ZrN-MoSN composite films with varying (Mo + S)/Zr ratios were deposited by fixing the Zr target power at 200 W and adjusting the MoS2 target power to 0, 30, 50, 80, 100, and 120 W, respectively. Throughout the deposition process, the substrate bias was maintained at −20 V, and the substrate temperature was kept at 200 °C. The total deposition time for each sample was 120 min. Additionally, a Mo-S-N reference film was deposited under the same deposition parameters.

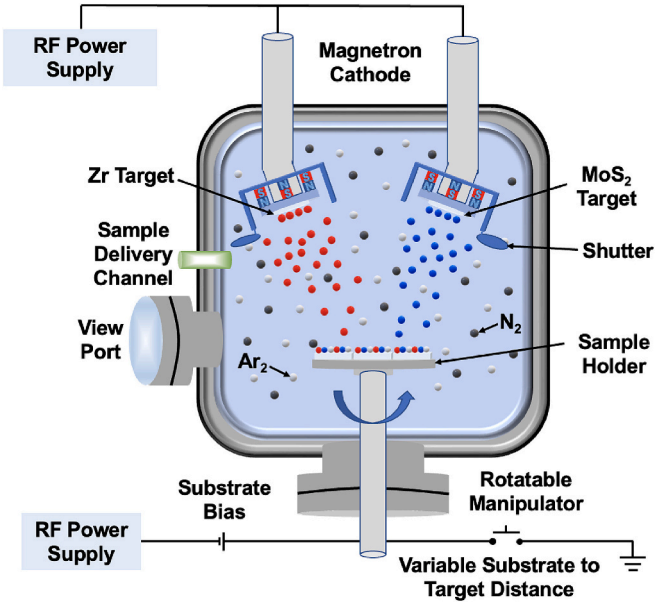

Fig. 1. 3D schematic representation of the magnetron sputtering machine for deposition of ZrN-MoSN films.

2.2. Microstructure and performance measurements

All microstructural and mechanical measurements were carried out using the samples on the wafer silicon substrates. The elemental composition of the ZrN-MoSN composite film was analyzed using an energy spectrometer (EDS, Inca X-Max50, Oxford, UK). An X-ray diffractometer (XRD, Shimazu-6000, Shimadzu, Japan) was used to characterize the crystal structure of the film. The main parameters used are as follows: (1) Cu Kα is the X-ray source, and the passing energy is 160 eV; (2) The 2θ angle range is 30–80°, and the scanning speed is 4°/min. An X-ray photoelectron spectrometer (XPS, ESCALAB250XI, Thermo Fisher, USA) was used to characterize the chemical bonds of the film, and the C 1s peak at 284.8 eV was used as the reference peak to correct the XPS spectrum. Before characterization, the sample was etched to remove the influence of surface oxidation on the test results. The specific etching parameters are as follows: the contaminant of sample surface was removed using a gentle Ar^+ beam, sputtering at a primary energy of 800 eV at an angle of ~70° from the surface normal held for 5 min, after the base pressure was below 2×10^{-9} mbr. The deconvolution of spectra was performed using the XPS CASA software, in which an adjustment of the peaks was performed using peak fitting with Gaussian–Lorentzian peak shape and Shirley type background subtraction.

The nano-indentation test was carried out using the samples on the wafer silicon substrates. A nano-indentation tester (NHT, CPX + NHT2 + MST, Anton Paar, Switzerland) equipped with a diamond Berkovich indenter was used to characterize the film hardness and elastic modulus. The specific parameters were as follows: (1) Maximum loading force was 3 mN; (2) Holding time was 10 s; (3) Loading and unloading speed was 0.1 mN/s. To ensure the accuracy of the test data, 2 different areas were selected on the sample surface and 15 measurements were performed respectively, and the average value was taken.

The W18 coated specimen was utilized to investigate the tribological properties, for providing insights relevant to industrial applications. The tests were performed on a ball-disk high-temperature friction and wear tester (UMT, UMT-2, CETR, USA) to study the friction and wear performance of the films at room temperature and high temperature environments. The test parameters are as follows: (1) The rotation speed was 50 rpm; (2) The normal load was 2 N and its corresponding pressure during the tribo-testing was around 2.9×10^4 N/m^2; (3) The test time

was 20 min; (4) The relative humidity of the environment was about 30 % for the tribo-testing at room temperature; (5) The counter friction pair was an alumina ball with a diameter of 9.4 mm. The roughness and hardness of the counterpart was below 0.05 μm, and 92 HRC, respectively. The average value of the long-term stable state in the friction curve is taken as the average friction coefficient of the film. The average cross-sectional area of the wear scars was measured using a probe profilometer (Dektak, Diktat-XT, Bruker, Germany). Following the tribo-testing, the wear track of each specimen was uniformly divided into six sections, and its corresponding 2D morphology was examined using the profilometer. Subsequently, the average integrated area was calculated and the wear rate was obtained according to the Archard's formula. Raman spectrometer was used to characterize the tribo-phase from the center of the wear scar surface.

3. Results and discussion

3.1. Elemental compositions and microstructure

Table 1 presents the elemental compositions of the ZrN-MoSN composite films, which were deposited with increasing power on the MoS_2 target, under a fixed mixture of argon and nitrogen. As depicted in Table 1, the content of Zr and N gradually decreases with the increased power applied on the MoS_2 target, resulting in the increase of the Mo and S content, maintaining a stable ratio of S/Mo. As it is expected, there is an increase of the (Mo + S)/Zr ratio, due to the higher target power generating more sputtered material from the MoS_2 target in the plasma.

In addition, the oxygen content also increases, from approximately 3.4 at.% for the binary reference ZrN film to about 6.9 at.% for the ZrN-MoSN film with a (Mo + S)/Zr ratio of 1.76. This increase in oxygen within the film primarily originates from contamination on the target surface. Despite pre-deposition cleaning of the target, it is susceptible to oxidation due to residual oxygen or moisture in the chamber. Another contributing factor to the elevated oxygen content is the interaction of residual moisture/oxygen with the sputtered plasma in the chamber. Additionally, the oxidation of the specimen surface occurs upon exposure to air, particularly as the MoS_2 phase is relatively unstable and prone to oxidation upon contact with oxygen and moisture in the atmosphere [25].

Moreover, the table illustrates the thickness of the film as a function of the MoS_2 target power, showing a slight increase with the higher MoS_2 target power due to the increased sputtered plasma onto the substrate.

Fig. 2 illustrates the XRD diffraction patterns of the ZrN-MoSN composite films with varying (Mo + S)/Zr ratios, alongside the diffraction patterns of reference ZrN and MoSN films. The binary ZrN film displays a cubic structure with a single fcc-ZrN phase, evidenced by diffraction peaks located at approximately 34.4°, ~38.9°, ~56.8°, ~67°, and ~72.2°, corresponding to fcc-ZrN (111), (200), (220), (311), and (222) (JCPDF #74-1217), respectively. This result is in good agreement with that from our previous papers [26]. Additional peaks at approximately 33.3° and ~68.5° are attributed to the Si substrate, while those at ~34.8°, ~64.3°, and ~72.5° arise from the Zr interlayer.

In the case of the MoSN reference film, two low-intensity diffraction peaks (as shown in the inset figure of Fig. 1) are assigned to hcp-MoS_2 (100) and (102) at approximately 30.3° and ~34.1° (JCPDF #74-0932), respectively. The introduction of nitrogen into the MoS_2 matrix weakens the crystalline quality, either through substitution of N into the S in the MoS_2 lattice (Mo(SN)$_x$) [27], or by forming a special microstructure of N_2 encapsulating the MoS_2 ($MoS_2(N_2)$) [28]. This results in a hindrance to the formation of a crystalline lamellar structure, leading to decreased diffraction peak intensity [29]. An intense diffraction peak at ~68.5°, attributed to the silicon substrate, is also observed.

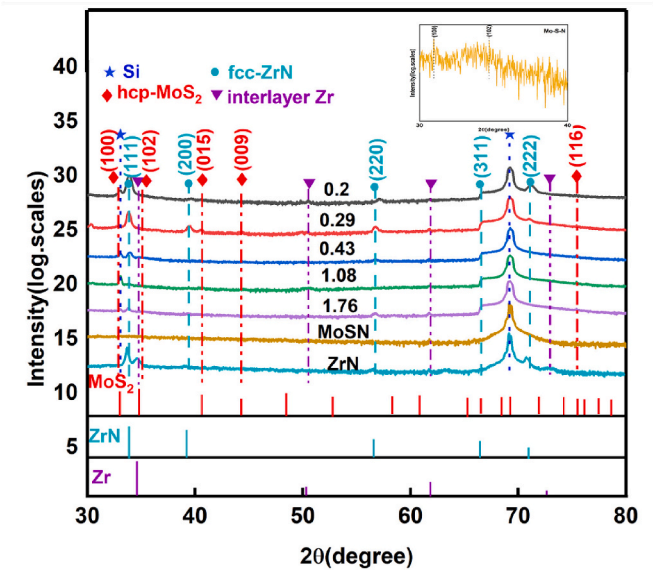

Fig. 2. XRD diffraction pattern of the ZrN-MoSN composite films with various (Mo + S)/Zr ratios, as well as the ZrN and MoSN reference films.

The ZrN-MoSN composite films, regardless of the (Mo + S)/Zr ratios, exhibits a polycrystalline structure consisting of fcc-ZrN and hcp-Mo(SN)$_x$, as indicated by the XRD pattern. Increasing the (Mo + S)/Zr ratios significantly weakens the intensity of all diffraction peaks in the as-deposited films, indicating an increased concentration of amorphous phases and the formation of nano-crystalline ZrN and MoS_2 embedded within the amorphous phase. This experimental phenomenon has also been observed in other nitride-based film systems, like Mo_2N-SiN_x [30], W_2N-SiN_x [31,32]. Notably, the primary diffraction peaks associated with fcc-ZrN planes in the XRD patterns of ZrN-MoSN composite films are consistently positioned at higher angles compared to those of the reference ZrN film. This observation suggests a lattice contraction, attributed to the solid solution of Mo or S into the ZrN lattice.

The cross-sectional characteristics of the ZrN-MoSN composite films, influenced by the (Mo + S)/Zr ratio, are presented in Fig. 3. The total thickness of the film, whether with a (Mo + S)/Zr ratio of 0.20 or 1.08, reaches approximately 2 μm. Both SEM images distinctly show a discernible interface between the as-deposited film and the wafer silicon. This corroborates the appearance of diffraction peaks from the Zr interface and Si substrate. The morphology depicted in both SEM images reveals a dense structure with classical columnar characteristics typical

Table 1
Elemental compositions and the (Mo + S)/Zr ratio of the ZrN-MoSN composite film as a function of MoS_2 target power.

	Elemental compositions (at.%)					(Mo + S)/Zr	Film thickness (μm)
	Zr	Mo	S	N	O		
0	52.8 ± 0.5	0	0	43.8 ± 0.5	3.4 ± 0.5	0	2.0 ± 0.1
30	46.1 ± 0.5	3.6 ± 0.5	5.5 ± 0.5	40.6 ± 0.5	4.2 ± 0.5	0.2 ± 0.5	2.0 ± 0.1
50	42.8 ± 0.5	4.9 ± 0.5	7.4 ± 0.5	39.6 ± 0.5	5.3 ± 0.5	0.29 ± 0.5	2.0 ± 0.1
80	37.4 ± 0.5	6.3 ± 0.5	9.6 ± 0.5	40.9 ± 0.5	5.8 ± 0.5	0.43 ± 0.5	2.0 ± 0.1
100	30.8 ± 0.5	13.2 ± 0.5	20 ± 0.5	29.5 ± 0.5	6.4 ± 0.5	1.08 ± 0.5	2.1 ± 0.1
120	26.2 ± 0.5	18.3 ± 0.5	27.8 ± 0.5	20.8 ± 0.5	6.9 ± 0.5	1.76 ± 0.5	2.1 ± 0.1

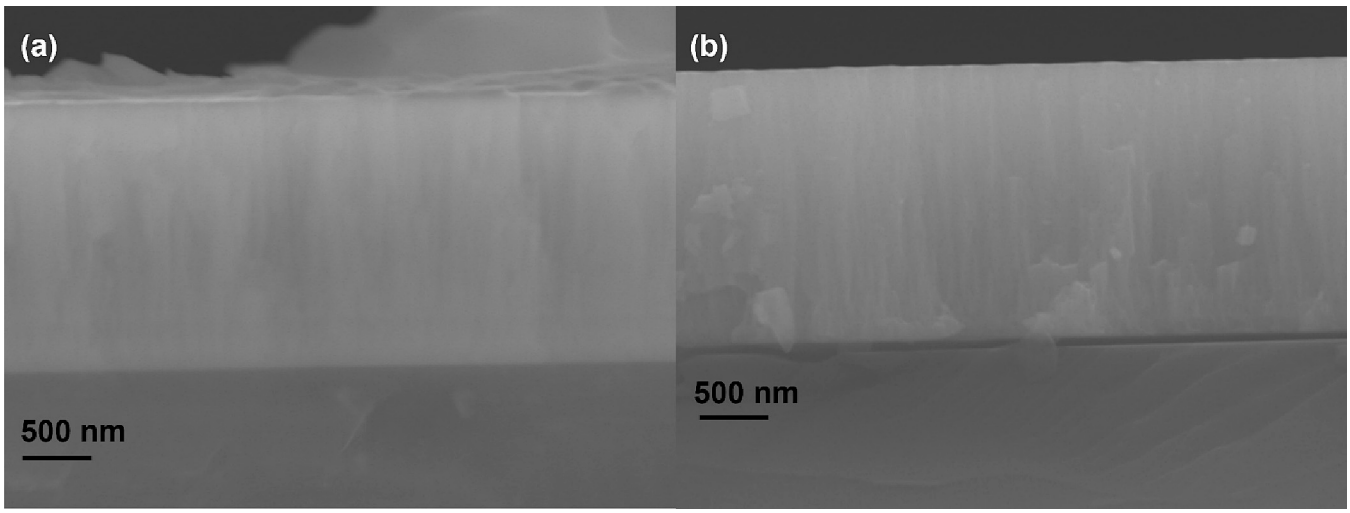

Fig. 3. The cross-sectional SEM image of the ZrN-MoSN composite film with the (Mo + S)/Zr ratio of 0.20 (a) and 1.08 (b).

of sputtered hard films, such as TiN [33], ZrN [34–36], or DLC [37–39].

Fig. 4 illustrates the XPS spectra of the film with various (Mo + S)/Zr ratios. The comprehensive XPS data, including Binding Energy (BE) positions, Full Width at Half Maximum (FHWM), and peak assignments is summarized in Table 2. Five main elements were detected in the overall XPS survey spectra, as depicted in Fig. 4(a), with C 1s serving as the reference peak for calibration, and the others originating from the as-deposited films. The Zr 3d high-resolution spectrum of the film, presented in Fig. 4(b), displays four split peaks assigned to two kinds of bonds, Zr—N (~182.0 and ~184.2 eV) [40] and Zr—O (~183.8 and ~186.4 eV) [41], respectively. Additionally, the increased (Mo + S)/Zr ratio results in peak shifting to higher binding energy and a drop in the relative intensity of the aforementioned four peaks. The observed high-energy shifting is attributed to the solid solution of Mo and S with a smaller radius into the ZrN lattice, a phenomenon also reported in Zr-Mo-N films deposited by magnetron sputtering [42]. The reduction in relative Zr content in the film, caused by an increase in MoS_2 target power, leads to a decrease in the relative intensity of peaks. As shown in Fig. 4(c), the Mo 3d spectra of the film exhibit four peaks assigned to Mo-S (~229.4 and ~230.0 eV) [43], Mo-N (~232.8 and ~233.0eV) [44], and Mo-O (~236.2 and~236.6 eV) [45] and S2s (~226.0 and ~226.2eV), respectively. The Mo-S-N film, deposited by sputtering MoS_2 target in a mixture of nitrogen and argon, can adopt a reported structure comprising a nano-crystalline phase embedded within an amorphous matrix. In this configuration, the nanoparticles of the MoS_2 phase are incorporated into the amorphous Mo(SN)$_x$ and $MoS_2(N_2)$ matrix [46]. The Mo-S-N phase tends to increase with higher (Mo + S)/Zr ratios, leading to stronger intensity in the Mo 3d peaks. The split two peaks in the S 2p spectrum at 161.6 and163.2 eV, as shown in Fig. 4(d), correspond to the Mo—S [47] and S—N [48] bonds, respectively, consistent with the Mo 3d results (Fig. 4c). The high-energy shift with the increase of (Mo + S)/Zr ratio is also related to the increased relative content of Mo-S-N, as discussed in the Mo 3d part. Fig. 4(e) depicts the N 1s XPS spectrum of the films, with three main peaks assigned to the N 1s, split into four peaks at ~401.0, ~396.2, ~399.0, and ~402.4 eV, corresponding to Zr—N [49], Mo—N [50], S—N [51], and N—N [52], respectively, apart from the peak at ~394.0 eV from Mo 3p3/2. The oxidation phase present in the film primarily comprises MoO_3 and ZrO_2, with two split peaks in the O 1s spectrum at ~530.2 and ~532.2 eV corresponding to Mo—O in MoO_3 [53] and Zr—O in ZrO_2 [54], respectively.

Based on the experimental results, multi-phase of fcc-ZrN, hcp-MoS_2, as well as the amorphous Mo(SN)$_x$ and $MoS_2(N_2)$, coexist in the films.

3.2. Mechanical properties

In Fig. 5 (a), the load-unloading curves of the film, characterized by varying (Mo + S)/Zr ratios, are depicted. It is evident that the maximum depth of the curves displays a notable dependence on the (Mo + S)/Zr ratios, with all values remaining below 10 % of total thickness, indicating a limited influence from the silicon wafer substrate.

Fig. 5 (b) shows the hardness and elastic modulus of the ZrN-MoSN film with various (Mo + S)/Zr ratios. The hardness and elastic modulus of the binary ZrN film are approximately 24 and ~276 GPa, respectively. The hardness of the ZrN-MoSN film gradually decreases to around ~10 GPa with an increase of the (Mo + S)/Zr ratio from 0.20 to 0.43. Subsequently, the hardness of the film exhibits a very small decrease with the (Mo + S)/Zr ratio, stabilizing at approximately 9 GPa for films with a (Mo + S)/Zr ratio of 1.76.

While the incorporation of either Mo or S into the ZrN lattice can induce solid solution strengthening, this effect is counteracted by the softening influence of Mo-S-N (below 10 GPa under the same deposition conditions [55]). Consequently, the overall hardness of the film diminishes with an increase in the (Mo + S)/Zr ratio. As a result, the film's hardness closely aligns with that of the Mo-S-N film, owing to the substantial formation of Mo-S-N within the composite. Therefore, the rule-of-mixture can be regarded as the primary determinant of the film's hardness.

The elastic modulus of the ZrN-MoSN films as a function of (Mo + S)/Zr ratio could be divided into three stages: (i) a stable value of ~280 GPa with the (Mo + S)/Zr ratio below 0.20, (ii) a decreasing value from ~280 to ~160 GPa with the (Mo + S)/Zr ratio from 0.20 to 0.43, and (iii) a stable value of ~150 GPa with the (Mo + S)/Zr ratio above 0.43. The solid solution of Mo and S into the ZrN lattice shortens the bonding length and thereby offsets the degrading effect from the Mo-S-N agent with low mechanical strengthening (its elastic modulus below 100 GPa [56]) in stage (i). Then, the gradual increase of the Mo-S-N phase weakens the overall elastic modulus of the film (in stage ii), ultimately resulting in a value similar to that of pure Mo-S-N in stage (iii).

3.3. Tribological properties at both room temperature and 500 °C

Some representative room temperature (RT) friction curves of the ZrN-MoSN film with various (Mo + S)/Zr ratios are shown in Fig. 6(a). All curves could be divided into two stages of the running-in period and the stationary plateau. At the beginning of the wear test, the asperities on the film surface initially contact the counterpart under the lubricating agents of moisture/oil absorbed on the film surface. This results in a

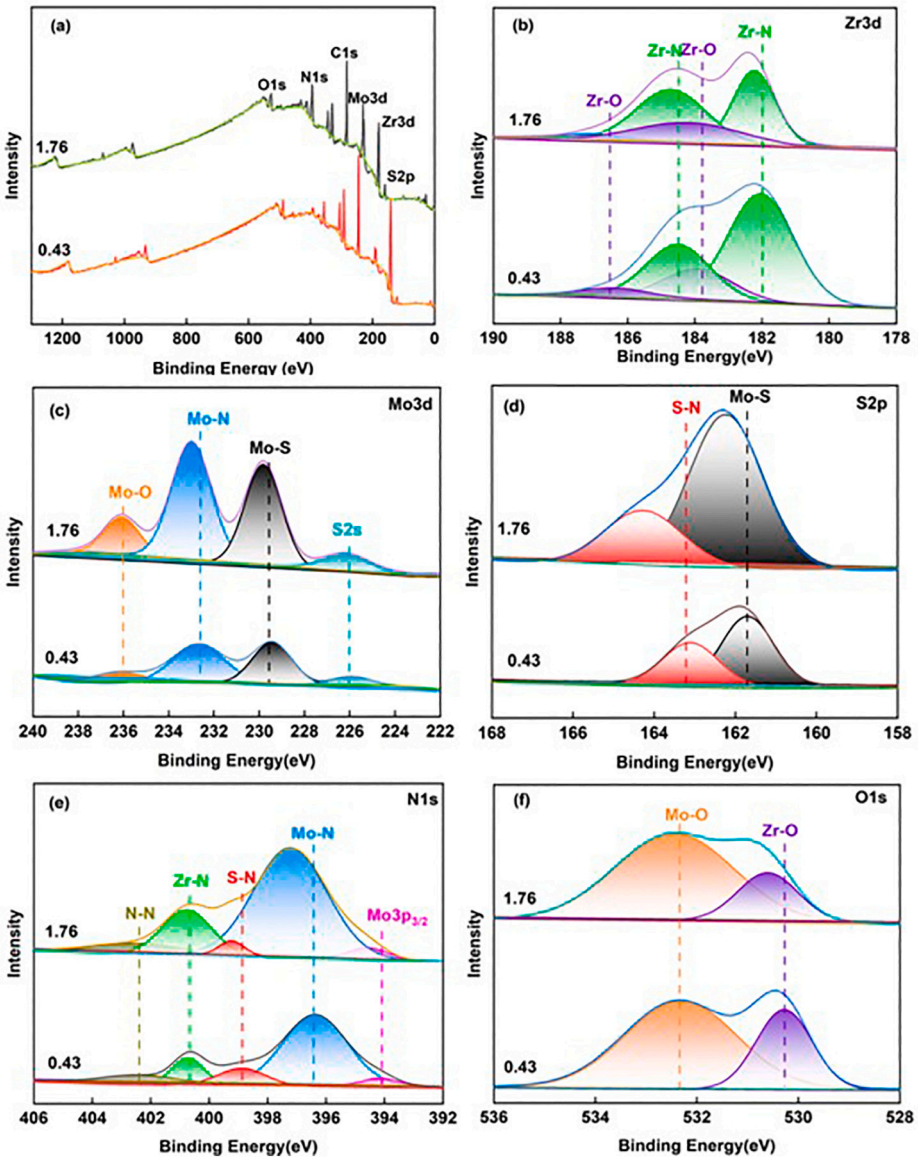

Fig. 4. XPS spectra of the ZrN-MoSN composite films with various (Mo + S)/Zr ratios: (a) full scanning spectra, and high-resolution ones of (b) Zr 3d, (c) Mo 3d, (d) S 2p, (e) N 1 s, and (f) O 1 s.

Table 2
The summarized XPS data of the ZrN-MoSN composite films with various (Mo+S)/Zr ratios.

	Peak assignments	B.E positions (eV)		FWHM (eV)
		(Mo+S)/Zr ratio: 0.43	(Mo+S)/Zr ratio: 1.76	
Zr 3d	Zr-N:2	184.2/182.0	182.2/184.6	0.68
	Zr-O:2	183.8/186.4	184.0/187.0	0.63
Mo 3d	Mo-O:1	236.2	236.6	0.86
	Mo-N:1	232.8	233.0	0.65
	Mo-S:1	229.4	230.0	0.42
	S2*s*:1	226.0	226.2	0.52
S 2p	Mo-S:1	161.6	162.2	1.17
	S-N:1	163.2	164.2	1.38
	$Mo3p_{3/2}$:1	394.0	394.2	1.36
N 1s	Mo-N:1	396.2	397.0	1.38
	S-N:1	399.0	399.4	1.40
	Zr-N:1	401.0	401.2	1.76
	N-N:1	402.4	402.8	1.20
O 1s	Mo-O:1	532.2	532.4	1.33
	Zr-O:1	530.2	530.6	1.26

gentle friction force and a relatively low friction coefficient (around ~0.20 in the figure) during this period. Subsequently, brittle and hard particles (e.g., ZrN phase) are easily crushed under the load, moving along with the counterpart to scratch/polish the wear track under the shear force, accumulating in front of the counterpart (see Fig. 7), and forming initial wear debris either on the wear track surface or on both sides of the track during sliding. This sharp increase in the friction coefficient from ~0.20 at the beginning to a maximum value of ~1.11 is observed. The depletion of the lubricant moisture/oil also contributes to the significant increase in the friction coefficient during this time. Following this, the friction coefficient gradually decreases over testing time. Although the maximum value of the friction coefficient during the running-in period is almost the same, the time to reach it depends on the (Mo + S)/Zr ratio: from ~170 s with a (Mo + S)/Zr ratio of 0.20 to ~40 s with a (Mo + S)/Zr ratio of 0.43, and then to ~100 s with a (Mo + S)/Zr ratio of 1.76. The decrease in hard debris, which could incrust the wear track surface, is reasonable with the (Mo + S)/Zr ratio (due to the drop in ZrN content based on Table 1 and Fig. 2), thereby shortening the time to reach the maximum friction coefficient. However, further increases in the (Mo + S)/Zr ratio degrade mechanical strengthening (resulting in

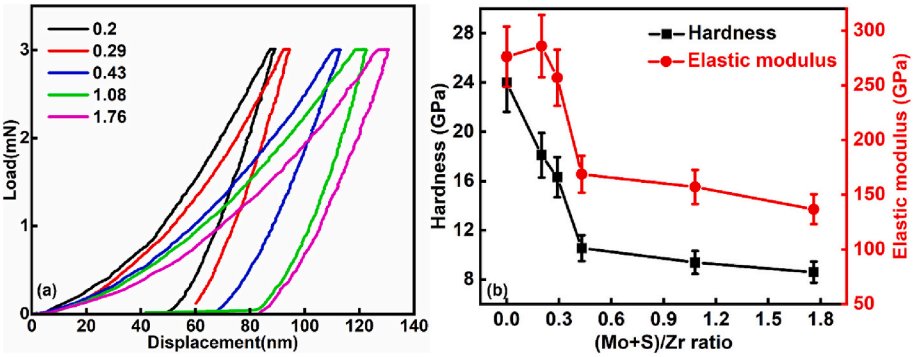

Fig. 5. The load-unloading curves (a), hardness and elastic modulus (b) of the ZrN-MoSN film with various of (Mo + S)/Zr ratios.

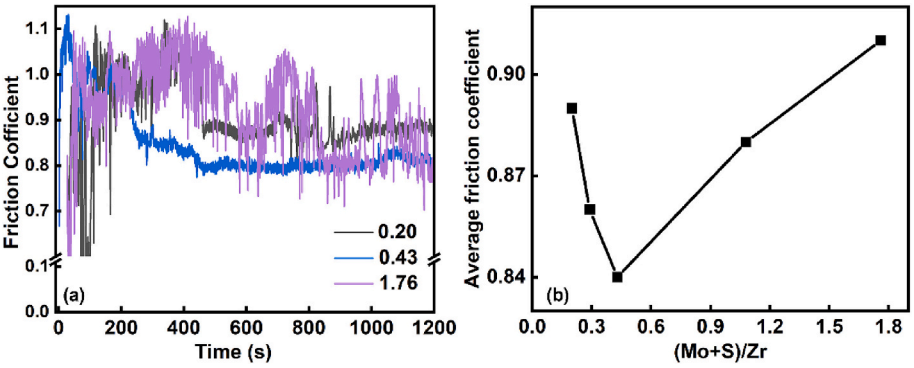

Fig. 6. Friction curve (a) and average friction coefficient (b) of ZrN-MoSN film with various (Mo + S)/Zr ratios.

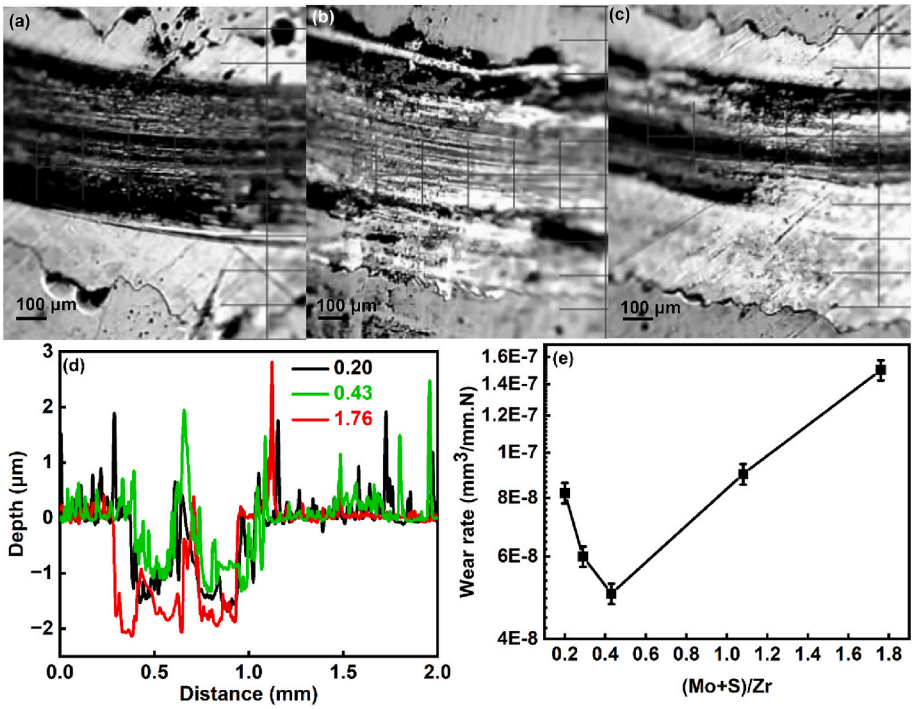

Fig. 7. Optical image of the wear track surface with the (Mo + S)/Zr ratio of 0.20 (a), 0.43 (b), and 1.76 (c), and its corresponding 2D morphology (d), the wear rate of the film with various (Mo + S)/Zr ratios (e), after the wear test at room temperature.

low load bearing capacity during sliding), broadening the contact area with the counterpart, and consequently increasing the time to reach the maximum friction coefficient during the running-in period. Following the running-in period is the stable period, during which a relatively stable friction coefficient as a function of testing time is observed. This stability arises from the film being fully contacted by the counterpart and the dynamic equilibrium relationship between the formation and consumption of wear debris. However, for the film with a (Mo + S)/Zr

ratio of 1.76, the friction coefficient fluctuates intensely with increasing testing time. Fig. 6(b) presents the average friction coefficient (COF) of the film as a function of (Mo + S)/Zr ratio. The results show a slight dependence on the (Mo + S)/Zr ratio: (i) COF initially decreases from ~0.89 with a (Mo + S)/Zr ratio of 0.20 to ~0.84 with a (Mo + S)/Zr ratio of 0.43, (ii) and then gradually increases to a maximum value of ~0.93 with an increase in the (Mo + S)/Zr ratio. Consequently, the optimized film with a (Mo + S)/Zr ratio of 0.43 is concluded to exhibit the shortest running-in period, as well as the most stable and lowest friction coefficient in the stable period.

Fig. 7 (a-d) presents the room temperature (RT) wear track optical morphologies of the film and their corresponding 2D profiles. In Fig. 7(a, d), the film with a (Mo + S)/Zr ratio of 0.20 is nearly worn out, with a depth of approximately 1.4 μm, which is close to the total thickness of the film. The width of the wear track is ~800 μm, and numerous fine scratches are evident. There is a noticeable accumulation of wear debris, both in the center and on both sides of the wear track. For the wear track of the film with a (Mo + S)/Zr ratio of 0.43, it exhibits the narrowest and shallowest morphology, with a width and depth of approximately 780 μm and 1.0 μm, respectively. While there is still observed accumulation of wear debris on both sides and the center of the wear track, the number of fine scratches is reduced. This suggests a gentler interaction between the counterpart and wear track due to the reduced presence of hard wear debris, resulting in a decrease in COF. Increasing the (Mo + S)/Zr ratio to 1.76 broadens the contact area due to the degradation of mechanical strengthening, leading to the zone near the sides of the wear track being worn out (with a depth deeper than the thickness). However, a smooth wear track surface with no obvious scratches is detected in this case. The wear rate (WR) of the films is shown in Fig. 7(e), where its value gradually decreases as the (Mo + S)/Zr ratio increases to 0.43, and then increases with further increases in the (Mo + S)/Zr ratio, after reaching a minimum value of approximately 5.1×10^{-8} mm^3/mm.N. The decrease in COF contributes to enhanced wear resistance for the film with a (Mo + S)/Zr ratio increasing from 0.20 to 0.43. However, the degradation of mechanical strengthening weakens the load-bearing capacity, resulting in poor wear resistance as the (Mo + S)/Zr ratio exceeds 0.43.

In Fig. 8(a), representative friction curves of the films during the 500 °C wear test are depicted. The friction coefficient at the beginning of the running-in period exhibits a high value of above 0.70 for the film with a (Mo + S)/Zr ratio below 0.43. It gradually drops with increased testing time, eventually reaching a relatively stable value in the stable period. However, distinguishing between the running-in and stable periods was not possible until the sliding test exceeded 600 s for the film with a (Mo + S)/Zr ratio of 1.76. After this point, a sharp increase in friction coefficient could be observed. The asperities on the wear track surface, which initially contact the counterpart, are squashed under the load, and move along with the counterpart during sliding. Consequently, hard debris such as ZrN and ZrO_2 (as observed in the Raman part) scratch the wear track surface, leading to a higher friction force and resulting in the high friction coefficient at the beginning of the running-in period. The decrease in the relative ZrN phase with increasing (Mo + S)/Zr ratio explains the disappearance of the high friction coefficient at the beginning of the running-in period. The dynamic equilibrium of the tribo-phase formation and consumption contributes to the stable friction coefficient in the stable period, as discussed in the RT tribological part. The trend of COF with increased (Mo + S)/Zr ratio is shown in Fig. 8(b): its value firstly decreases from around 0.38 with a (Mo + S)/Zr ratio of 0.20 to about 0.29 with a (Mo + S)/Zr ratio of 0.43, and then remains stable until reaching the maximum (Mo + S)/Zr ratio of 1.76 with the COF of approximately 0.20. The 2D wear track morphology of the film with various (Mo + S)/Zr ratios is shown in Fig. 8(c). A shallow wear track with a width of ~700 μm is observed for the film with a (Mo + S)/Zr ratio of 0.20. There is a deep scratch at the center of the track, resulting from the hard debris. Increasing the (Mo + S)/Zr ratio to 0.43 leads to the disappearance of the deep scratch, but the wear track surface still exhibits a coarse morphology due to the large number of fine scratches. The wear track is very shallow, resulting in an extremely low WR of $\sim 7.2 \times 10^{-9}$ mm^3/mm.N. A gentle interaction between the film and counterpart induced by the low COF (~0.29), as well as the accumulation of wear debris, contributes to the excellent wear-resistance

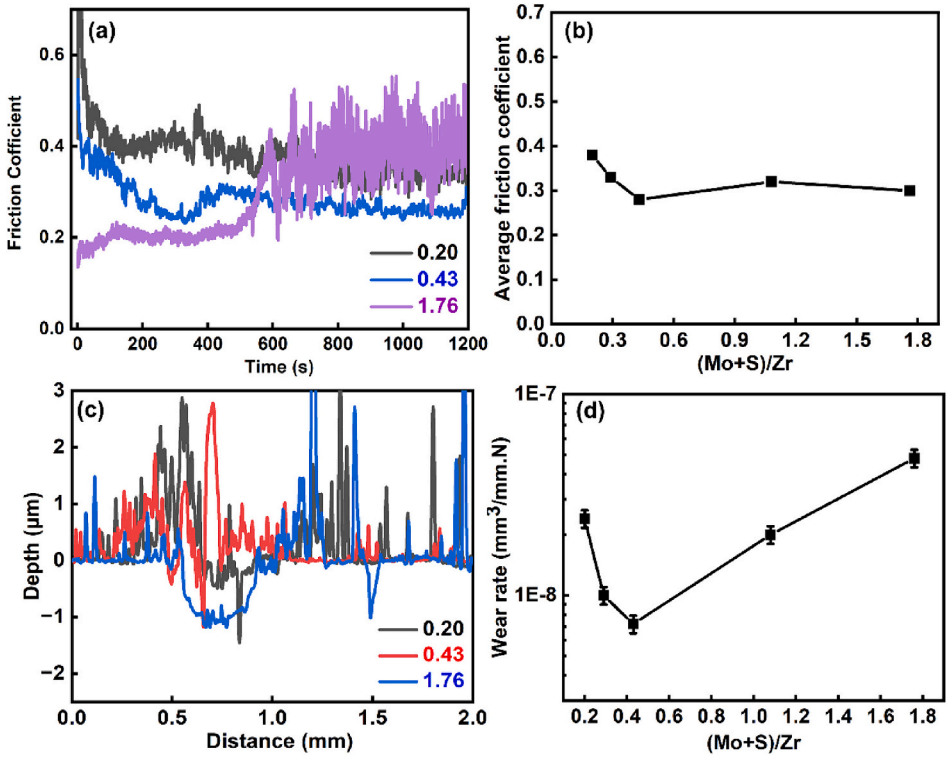

Fig. 8. The friction coefficient curve (a), the average friction coefficient (b), 2D wear track morphology (c) and wear rate of the ZrN-MoSN film with various (Mo + S)/Zr ratios, after the 500 °C wear test.

properties. Further increase in the (Mo + S)/Zr ratio to 1.76 broadens and deepens the wear track, but the maximum depth is still below the total thickness of the film, indicating it is not worn out. The 500 °C WR, as shown in Fig. 8(d), is significantly influenced by the (Mo + S)/Zr ratio. Its value is ~2.5 × 10^{-8} mm^3/mm.N with a (Mo + S)/Zr ratio of 0.20 and decreases with increasing (Mo + S)/Zr ratio. Wear resistance is extremely enhanced as the (Mo + S)/Zr ratio increases to 0.43. However, WR increases with further increases in the (Mo + S)/Zr ratio, ultimately leading to a maximum WR for the film with a (Mo + S)/Zr ratio of 1.76.

Tribo-phases formed during sliding, arising from complex tribo-chemical reactions under the influence of counterpart forces (load and shear), have been extensively documented for their significant impact on tribological behaviors [57–59]. Consequently, Raman spectra obtained from the wear track surface of the film with a (Mo + S)/Zr ratio of 0.43 are presented in Fig. 9. The spectra of the as-deposited film and the magnetron-sputtered MoS_2 film are included in this figure to elucidate the evolution of the tribo-phase following room temperature (RT) and 500 °C wear tests. Two peaks at about 372 and 410 cm^{-1}, corresponding to E^1_{2g} and A_{1g} phonon of well-ordered MoS_2 respectively [60], are observed in the sputtered MoS_2 film. However, both peaks are all disappeared in the as-deposited ZrN-MoSN film spectra. Incorporation of nitrogen into the MoS_2 effectively hinders the lamellar structure through the formation of amorphous or poor crystalline Mo $(SN)_x$ or $MoS_2(N_2)$ and, thereby resulting in the disappearance of the E^1_{2g} and A_{1g} Raman peaks. Although the reorientation of MoS_2 paralleling to the sliding direction induced by the load/shear force was widely reported in some MoS_2 or WS_2 based film [61,62], there is no obvious peaks referring to the MoS_2 after the RT wear test. As for the spectrum from 500 °C wear track, there are ten Raman peaks corresponding to MoO_3 and ZrO_2 respectively, based on the Refs. [63, 64]. The main tribo-phase could be the MoO_3, from the oxidized Mo-S-N phase, due to all Raman peaks with high intensity belonging to this phase. Layered MoO_3 is the well-known self-lubricant tribo-phase to enhance the friction performance [65]. However, ZrO_2 constitutes the hard phase, resulting in the hard friction phase moving with the friction pair and causing scratches and wear marks.

Based on the experimental results, both mechanical properties and the presence of tribo-phases significantly influence the tribological behaviors observed. At room temperature (RT), the lubricant mechanism of MoS_2-based agents involves the reorientation of the lamellar MoS_2 phase under the load/shear force from the counterpart, aligning parallel to the sliding direction [66]. However, the incorporation of nitrogen into the MoS_2 structure hinders the formation of well-ordered MoS_2 phases, thereby degrading the lubricant properties. Consequently, the (Mo + S)/Zr ratio exhibits only a slight effect on the anti-frictional properties, with the coefficient of friction (COF) decreasing marginally from 0.89 to 0.84 as the (Mo + S)/Zr ratio increases from 0.20 to 0.43. The reduction in hardness weakens the load-bearing capacity, leading to a broadened contact area and subsequently an increased COF with further increases in the (Mo + S)/Zr ratio. The combined influence of anti-frictional and mechanical properties contributes to slightly enhanced wear resistance when the (Mo + S)/Zr ratio reaches 0.43. At 500 °C, the dominant tribo-phase of MoO_3 with a layered structure significantly affects frictional behaviors, and friction oxidation can be considered the primary wear mechanism at this temperature. The formation of layered MoO_3 effectively reduces the COF with increasing (Mo + S)/Zr ratio. However, the poor thermal stability of Mo-S-N, which is reported to be totally oxidized above 400–600 °C, contributes to increased wear rate (WR). Although the hard ZrO_2 tribo-phase can cause deep scratches on the wear track surface by moving along with the counterpart, it enhances the mechanical strength of wear debris, benefiting the wear resistance properties. Additionally, the presence of the hard ZrN phase with relatively good thermal stability also contributes to enhanced wear resistance properties. Therefore, the enhanced wear resistance properties observed with increasing (Mo + S)/Zr ratio from 0.20 to 0.43 can be attributed to (i) improved anti-frictional properties, (ii) the presence of sufficient hard ZrO_2 tribo-phase, and (iii) the presence of ZrN phase in the film. However, the extensive oxidation of the Mo-S-N phase is the primary factor degrading wear resistance for films with a (Mo + S)/Zr ratio above 0.43.

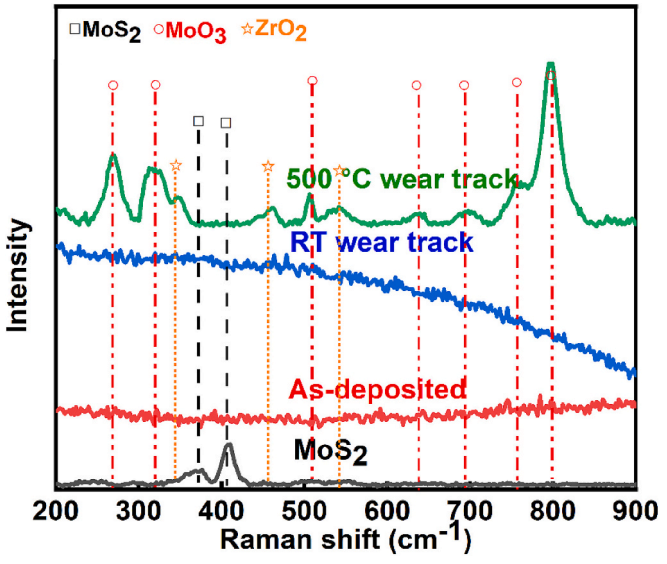

Fig. 9. Raman spectra of the magnetron sputtered MoS_2, as-deposited ZrN-MoSN film with the (Mo + S)/Zr ratio of 0.43, and its RT wear track, 500 °C wear track.

4. Conclusion

ZrN film, a quintessential nitride hard material, has been extensively engineered through composite systems to meet the rigorous demands of industrial applications. In this study, a series of ZrN-MoSN composite films were deposited using the magnetron co-sputtering, leveraging the hard structural matrix with the Mo-S-N self-lubricant agents. The influence of (Mo + S)/Zr ratio on the microstructure, mechanical and tribological (RT and 500 °C) properties was investigated, yielding the following key conclusions:

(1) Regardless of (Mo + S)/Zr ratio, ZrN-MoSN composite films exhibited a dense columnar structure, with a mixture phase of fcc-ZrN, hcp-MoS_2, and amorphous phases of Mo $(SN)_x$ and $MoS_2(N_2)$.

(2) The mechanical strength decreased with increasing (Mo + S)/Zr ratio due to the softer nature of the Mo-S-N phases. The elastic modulus initially remained stable with (Mo + S)/Zr ratio below 0.20, attributable to the solid solution of Mo and S into the ZrN lattice counteracting the degradation from the Mo-S-N phase, followed by a gradual decrease.

(3) The incorporation of nitrogen into the MoS_2 inhibited its well-ordered structure, mildly affecting room temperature tribological properties. However, the synergistic effects of the ZrN matrix and the tribo-phases of layered MoO_3 and hard ZrO_2 significantly enhanced the tribological properties at 500 °C, achieving a coefficient of friction (COF) of approximately 0.29 and a minimum wear rate (WR) of approximately 7.2 × 10^{-9} mm^3/mm.N, particularly notable at a (Mo + S)/Zr ratio of 0.43.

CRediT authorship contribution statement

Jing Luan: Writing – review and editing, Writing – original draft, Investigation. **Hongying Lu:** Writing – original draft, Investigation. **Junhua Xu:** Resources, Project administration. **Filipe Fernandes:** Methodology, Data curation. **Manuel Evaristo:** Methodology, Data curation. **Bingyang Ma:** Methodology, Data curation. **Fuxiang Xie:** Methodology, Data curation. **Albano Cavaleiro:** Supervision. **Hongbo**

Ju: Writing – review & editing, Writing – original draft, Validation, Supervision, Resources, Project administration, Methodology, Investigation, Funding acquisition, Formal analysis, Data curation, Conceptualization.

Declaration of competing interest

We declare that we do not have any commercial or associative interest that represents a conflict of interest in connection with the work submitted.

Data availability

Data will be made available on request.

Acknowledgement

Supported by the National Natural Science Foundation of China with the number of 52171071 and 51801081, national funds through FCT of Portugal – Fundação para a Ciência e a Tecnologia, under a scientific contract of 2021.04115.CEECIND, 2023.06224.CEECIND, and the projects of UIDB/00285/2020, and LA/0112/2020.

References

[1] S.S. Perry, W.T. Tysoe, Frontiers of fundamental tribological research, Tribol. Lett. 19 (2005) 151–161.
[2] H. Ju, K. Huang, J. Luan, Y. Geng, J. Yang, J. Xu, Evaluation under temperature cycling of the tribological properties of Ag-SiN_x films for green tribological applications, Ceram. Int. 49 (2023) 30115–30124.
[3] M. Korkmaz, M. Gupta, N. Ross, V. Sivalingam, Implementation of green cooling/lubrication strategies in metal cutting industries: a state of the art towards sustainable future and challenges, Sustain. Mater. Technol. 36 (2023) e00641.
[4] M. Woydt, The importance of tribology for reducing CO_2 emissions and for sustainability, Wear 474-475 (2021) 203768.
[5] A.K. Bisht, R.O. Vaishya, R.S. Walia, G. Singh, Nitrides ceramic coatings for tribological applications: a journey from binary to high-entropy compositions, Ceram. Int. 50 (2024) 8553–8585.
[6] M.D. Jean, C.D. Liu, S.M. Chiu, T.H. Chien, Modelling, fabrication and optimization for hard coatings of deposited ceramic nitride films using a magnetron sputtering, Phys. Procedia 32 (2012) 289–296.
[7] H. Ju, L. Yu, D. Yu, I. Asempah, J. Xu, Microstructure, mechanical and tribological properties of TiN-Ag films deposited by reactive magnetron sputtering, Vacuum 141 (2017) 82–88.
[8] H. Ju, J. Xu, Microstructure, oxidation resistance, mechanical and tribological properties of Ti-Y-N films by reactive magnetron sputtering, Surf. Coat. Technol. 283 (2015) 311–317.
[9] H. Ju, L. Xu, J. Luan, Y. Geng, J. Xu, L. Yu, J. Yang, F. Fernandes, Enhancement on the hardness and oxidation resistance property of TiN/Ag composite films for high temperature applications by addition of Si, Vacuum 209 (2023) 111752.
[10] D. Roman, J. Bernardi, C.L.G. Amorim, F.S. Souza, A. Spinelli, C. Giacomelli, C. A. Figueroa, I.J.R. Baumvol, R.L.O. Basso, Effect of deposition temperature on microstructure and corrosion resistance of ZrN thin films deposited by DC reactive magnetron sputtering, Mater. Chem. Phys. 130 (2011) 147–153.
[11] S. Zhang, J. Wang, R. Wong, L. Liu, B. Pan, C. Liu, Structural and corrosion resistance properties of sputtered zirconium nitride thin films as electrode materials for supercapacitor, J. Alloys Compd. 900 (2022) 163506.
[12] T. He, Z. Valery, A. Vereschaka, A. Keshin, Y. Huo, F. Milovich, C. Sotova, A. Seleznev, Influence of niobium and hafnium doping on the wear and corrosion resistance of coatings based on ZrN, J. Mater. Res. Technol. 27 (2023) 6386–6399.
[13] D. Valerini, M.A. Signore, L. Tapfer, E. Piscopiello, U. Galietti, A. Rizzo, Adhesion and wear of ZrN films sputtered on tungsten carbide substrates, Thin Solid Films 538 (2013) 42–47.
[14] T. Kuznetsova, V. Lapitskaya, A. Khabarava, S. Chizhik, B. Warcholinski, A. Gilewicz, The influence of nitrogen on the morphology of ZrN coatings deposited by magnetron sputtering, Appl. Surf. Sci. 522 (2020) 146508.
[15] V. Prysiazhnyi, J. Kratochvil, D. Kaftan, R. Ctvrtlik, V. Stranak, Growth of hard nanostructured ZrN surface induced by copper nanoparticles, Appl. Surf. Sci. 562 (2021) 150230.
[16] F. Cai, Q. Zhou, J. Chen, S. Zhang, Effect of inserting the Zr layers on the tribo-corrosion behavior of Zr/ZrN multilayer coatings on titanium alloys, Corros. Sci. 213 (2023) 111002.
[17] G.I. Nkou Bouala, A. Etiemble, S. Dassonneville, S. Dassonneville, C. Der Loughian, C. Langlois, J.F. Pierson, P. Steyer, Structural and microstructural evolution of amorphous Zr-Cu-Ag thin-film alloys under thermal constraint: an *in situ* approach, J. Alloys Compd. 851 (2021) 156908.
[18] H. Ju, D. Yu, J. Xu, L. Yu, B. Zuo, Y. Geng, T. Huang, L. Shao, L. Ren, C. Du, H. Zhang, H. Mao, Crystal structure and tribological properties of Zr-Al-Mo-N composite films deposited by magnetron sputtering, Mater. Chem. Phys. 230 (2019) 347–354.
[19] S. Dong, W. Cheng, J. Yao, Influence of reciprocating friction on friction and wear characteristics of MoS_2 films, Results Eng. 18 (2023) 1010173.
[20] Z. Yan, H. Zhou, X. Zhang, J. Liu, C. Wong, X. Lu, J. Hao, Xu. Sui, Interactive effect between WS_2 films with different structures and space oils for improvement of tribological performance, Tribol. Int. 170 (2022) 107431.
[21] C.C. Baker, J.J. Hu, A.A. Voevodin, Preparation of Al2O3/DLC/Au/MoS2 chameleon coatings for space and ambient environments, Surf. Coat. Technol. 201 (2006) 4224–4229.
[22] T.H. Dolla, T. Matthews, N.W. Maxakato, P. Ndungu, T. Montini, Recent advances in transition metal sulfide-based electrocatalysts and photocatalysts for nitrogen fixation, J. Electroanal. Chem. 928 (2023) 117049.
[23] L. Isaeva, J. Sundberg, S. Mukherjee, C.J. Pelliccione, A. Lindblad, C.U. Serge, U. Jansson, D.D. Sarma, O. Eriksson, K. Kadas, Amorphous W-S-N thin films: the atomic structure behind ultra-low friction, Acta Mater. 82 (2015) 84–93.
[24] H. Ju, R. Wang, N. Ding, L. Yu, J. Xu, F. Ahmed, B. Zuo, Y. Geng, Improvement on the oxidation resistance and tribological properties of molybdenum disulfide film by doping nitrogen, Mater. Des. 186 (2020) 108300.
[25] T. Sasikala, K. Shanmugasundaram, P. Thirunavukkarasu, P. Vivek, V. Balasubramani, Impact of phase transformation on MoS2 thin films on high temperature and its concomitant role in In-MoS_2/P-Si structured PN junction diodes, Opt. Mater. 131 (2022) 112584.
[26] H. Ju, D. Yu, L. Yu, N. Ding, J. Xu, X. Zhang, Y. Zheng, L. Yang, X. He, The influence of ag contents on the microstructure, mechanical and tribological properties of ZrN-Ag films, Vacuum 148 (2018) 54–61.
[27] X. Zhang, Z. Liu, X. Wei, S. Ali, J. Lang, B. Yang, R. Hu, J. Qi, X. Yan, Unraveling the improved lithium-storage mechanism by interfacial engineering based on metallic MoS_2/MoN heterostructure, J. Alloys Compd. 966 (2023) 171282.
[28] W. Tillmann, D. Kokalj, D. Stangier, Impact of structure on mechanical properties and oxidation behavior of magnetron sputtered cubic and hexagonal MoN_x thin films, Appl. Surf. Sci. Adv. 5 (2021) 100119.
[29] H. Ju, R. Wang, N. Ding, L. Yu, J. Xu, F. Ahmed, B. Zuo, Y. Geng, Improvement on the oxidation resistance and tribological properties of molybdenum disulfide film by doping nitrogen, Mater. Des. 186 (2020) 108300.
[30] H. Ju, R. Zhou, J. Luan, L. Yu, J. Xu, B. Zuo, J. Yang, Y. Geng, L. Zhao, F. Fernandes, Multilayer Mo_2N-Ag/SiNx films for demanding applications: morphology, structure and temperature-cycling tribological properties, Mater. Des. 223 (2022) 111128.
[31] H. Ju, X. He, L. Yu, J. Xu, The microstructure and tribological properties at elevated temperature of tungsten silicon nitride films, Surf. Coat. Technol. 326 (2017) 255–263.
[32] H. Ju, S. He, L. Yu, I. Asempah, J. Xu, The improvement of oxidation resistance, mechanical and tribological properties of W_2N films by doping silicon, Surf. Coat. Technol. 317 (2017) 158–165.
[33] E. Ramos-Moore, A. Rosenkranz, D.E. Diaz-Droguett, C. Espinoza, I. El Azahri, F. Mucklich, Influence of crystallographic texture on friction in a-Al_2O_3/Ti(C,N) ceramic tool coatings, Ceram. Int. 23 (2022) 34571–34575.
[34] F. Zhu, K. Zhu, Y. Hu, Y. Ling, D. Wang, H. Peng, Z. Xie, R. Yang, Z. Zhang, Microstructure and Young's modulus of ZrN thin film prepared by dual ion beam sputtering deposition, Surf. Coat. Technol. 374 (2019) 997–1005.
[35] S. Lin, J. Zhang, R. Zhu, S. Fu, D. Yun, Effects of sputtering pressure on microstructure and mechanical properties of ZrN films deposited by magnetron sputtering, Mater. Res. Bull. 105 (2018) 231–236.
[36] J. Huang, C. Ho, G. Yu, Effect of nitrogen flow rate on the structure and mechanical properties of ZrN thin films on Si(100) and stainless steel substrates, Mater. Chem. Phys. 102 (2007) 31–38.
[37] K. Bewilogua, D. Hofmann, History of diamond-like carbon films-from first experiments to worldwide applications, Surf. Coat. Technol. 242 (2014) 214–225.
[38] R. Hauert, An overview on the tribological behavior of diamond-like carbon in technical and medical applications, Tribol. Int. 37 (2004) 991–1003.
[39] O.D. Coskun, T. Zerrin, Optical, structural and bonding properties of diamond-like amorphous carbon films deposited by DC magnetron sputtering, Diam. Relat. Mater. 56 (2015) 29–35.
[40] P.C.S. Neto, F.G.R. Freitas, D.A.R. Fernandez, R.G. Carvalho, L.C. Felix, A.R. Terto, R. Huler, F.M.T. Mendes, A.H.S. Junior, E.K. Tentardini, Investigation of microstructure and properties of magnetron sputtered Zr-Si-N thin films with different Si content, Surf. Coat. Technol. 353 (2018) 353–363.
[41] Z.B. Qi, Z.T. Wu, H.F. Liang, D.F. Zhang, J.H. Wang, Z.C. Wang, In situ and ex situ studies of microstructure evolution during high-temperature oxidation of ZrN hard coating, Scr. Mater. 97 (2015) 9–12.
[42] V.F.D. Soares, D.A.R. Fernandez, A.S. Fontes Junior, R.G. Carvalho, R. Machado, F. M.T. Mendes, Structure and high temperature oxidation of $Zr_{(1-x)}Mo_{(x)}$ thin films deposited by reactive magnetron sputtering, Appl. Surf. Sci. 485 (2019) 490–495.
[43] Z. Duan, X. Zhao, J. Xu, P. Wang, W. Liu, Influence of Ni^{13+} ions irradiation on the microstructure, mechanical and tribological properties of Mo-S-Ti composite films, Appl. Surf. Sci. 480 (2019) 438–447.
[44] H. Ju, R. Wang, W. Wang, J. Xu, L. Yu, H. Luo, The microstructure and tribological properties of molybdenum and silicon nitride composite films, Surf. Coat. Technol. 401 (2020) 126238.
[45] Y. Sutou, S. Komiyama, M. Sonobe, D. Ando, J. Koike, M. Wang, Microstructure, hardness and wear resistance of reactive sputtered Mo-O-N films on stainless steel substrate, Surf. Coat. Technol. 280 (2015) 1–7.
[46] T. Hudec, T. Roch, M. Gregor, L. Orovcik, M. Mikula, T. Polcar, Tribological behaviour of Mo-S-N solid lubricant coatings in vacuum, nitrogen gas and elevated temperature, Surf. Coat. Technol. 405 (2021) 126722.

[47] A. Rasa, M. Yousaf, A. Rasheed, A. Farid, I.A. Khan, Synthesis of binder-free nanostructure MoS_2 films for optoelectronic applications, Phys. B Condens. Matter 670 (2023) 415350.
[48] N. Wei, H. Li, J. Li, L. Sun, J. Huang, J. Kong, Q. Wu, Y. Shi, D. Xiong, Structure, mechanical, tribological properties and corrosion resistance of C/N dual doping Mo-S-C-N films, Appl. Surf. Sci. 646 (2024) 158905.
[49] D.F. Zambrano-Mera, R. Espinoza-Gonzalez, R. Villarroel, A. Rosenkranz, N. Carvajal, M.I. Pintor-Monroy, A.G. Montano-Figueroa, M.J. Arellano-Jimenez, M. Quevedo-Lopez, P. Valenzuela, W. Gacitua, Optical and mechanical properties of Zr-oxide doped TiO_2/SiO_2 anti-reflective coatings for PV glass covers, Sol. Energy Mater. Sol. Cells 243 (2022) 111784.
[50] H. Ju, L. Yu, J. Xu, Synthesis and characterization of phase structures and properties of Mo-N coatings, Chin. J. Vac. Sci. Technol. 34 (2014) 469–472.
[51] T. Hudex, M. Mikula, L. Satrapinskyy, T. Roch, M. Truchly, P.S. Jr, T. Huminiuc, T. Polcar, Structure, mechanical and tribological properties of Mo-S-N sold lubricant coatings, Appl. Surf. Sci. 486 (2019) 1–14.
[52] J. Zhang, L. Yin, Microstructure and mechanical properties of (Ti,Al,Nb)N hard films with N-gradient distributions, Thin Solid Films 584 (2015) 141–145.
[53] Q. Han, R. Wang, H. Zhu, M. Wan, Y. Mai, The preparation and investigation of all thin film electrochromic devices based on reactively sputtered MoO_3 thin films, Mater. Sci. Semicond. Process. 126 (2021) 105686.
[54] S. Zuzjakova, P. Zeman, S. Haviar, R. Cerstvy, J. Houska, J. Rezek, J. Vlcek, Thermal stability of structure, microstructure and enhanced properties of Zr-Ta-O films with a low and high Ta content, Surf. Coat. Technol. 335 (2018) 95–103.
[55] K.H. Kannur, T. Huminiuc, T.B. Yaqub, T. Polcar, C. Pupier, C. Heau, A. Cavaleiro, An insight on the MoS_2 tribo-film formation to determine the friction performance of Mo-S-N sputtering coatings, Surf. Coat. Technol. 408 (2021) 126791.
[56] X. Zhang, L. Qiao, L. Chai, J. Xu, L. Shi, P. Wang, Structural, mechanical and tribological properties of Mo-S-N solid lubricant films, Surf. Coat. Technol. 296 (2016) 185–191.
[57] T. Weikert, S. Wartzack, M.V. Baloglu, K. Willner, S. Gabel, B. Merle, F. Pineda, M. Walczak, M. Marian, A. Rosenkranz, S. Tremmel, Evaluation of the surface fatigue behavior of amorphous carbon coatings through cyclic nanoindentaion, Surf. Coat. Technol. 407 (2021) 126769.
[58] H. Ju, R. Zhou, S. Liu, L. Yu, J. Xu, Y. Geng, Enhancement of the tribological behavior of self-lubricating nanocomposite Mo_2N/Cu films by adding the amorphous SiN_x, Surf. Coat. Technol. 423 (2021) 127565.
[59] H. Ju, J. Guo, L. Yu, J. Xu, J. Luan, Enhancement of the mechanical and tribological properties of self-lulbricant Mo_2N-Ag composite film by additing amorphous SiN_x, Ceram. Int. 50 (2024) 8463–8471.
[60] W.D. Sun, J. Wang, K.W. Wang, J.J. Pan, R. Wang, M. Wen, K. Zhang, Turbulence-like Cu/MoS_2 films: structure, mechanical and tribological properties, Surf. Coat. Technol. 422 (2021) 127490.
[61] A. Jiang, X. Cao, Z. Wang, J. Ma, J. Xiao, S. Ma, Friction performance and corrosion resistance of MoS2/DLC composite films deposited by magnetron sputtering, Results Phys. 25 (2021) 104278.
[62] G. Du, D. Ba, Z. Tan, K. Liu, Tribological behavior of RF sputtering WS2 thin films with vacuum annealing, Phys. Procedia 18 (2011) 256–260.
[63] A. Rizzo, M.A. Signore, D. Valerini, D. Altamura, A. Cappello, L. Tapfer, A study of suppression effect of oxygen contamination by bias voltage in reactively sputtered ZrN films, Surf. Coat. Technol. 206 (2012) 2711–2718.
[64] C. Liu, H. Ju, L. Yu, J. Xu, Y. Geng, W. He, J. Jiao, Tribological properties of Mo_2N films at elevated temperature, Coatings 9 (2019) 734.
[65] H. Ftouhi, H. Lamkaouane, G. Louarn, M. Diani, J. Bernede, M. Addou, L. Cattin, Low temperature synthesis of MoS2 and MoO3: MoS2 hybrid thin film via the use of an original hybrid sulfidation technique, Surf. Interfaces 32 (2022) 102120.
[66] A. Seynstahl, M. Kobrich, T. Rosnitschek, M. Goken, S. Tremmel, Enhancing the lifetime and vacuum tribological performance of PVD-MoS_2 coatings by nitrogen modification, Surf. Coat. Technol. 477 (2024) 130343.